
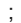



RESEARCH ARTICLE | MARCH 16 2023

Local electric field perturbations due to trapping mechanisms at defects: What random telegraph noise reveals

Sara Vecchi  ; Paolo Pavan  ; Francesco Maria Puglisi 



Journal of Applied Physics 133, 114101 (2023)

<https://doi.org/10.1063/5.0137245>



CrossMark

Articles You May Be Interested In

Random telegraph-signal noise in junctionless transistors

Appl. Phys. Lett. (March 2011)

Random telegraphic noise in double barrier systems

Appl. Phys. Lett. (November 1993)

Random telegraph noise in 2D hexagonal boron nitride dielectric films

Appl. Phys. Lett. (March 2018)



Time to get excited.
Lock-in Amplifiers – from DC to 8.5 GHz

[Find out more](#)

Local electric field perturbations due to trapping mechanisms at defects: What random telegraph noise reveals

Cite as: J. Appl. Phys. 133, 114101 (2023); doi: 10.1063/5.0137245

Submitted: 1 December 2022 · Accepted: 26 February 2023 ·

Published Online: 16 March 2023



Sara Vecchi, Paolo Pavan, and Francesco Maria Puglisi^{a)}

AFFILIATIONS

Dipartimento di Ingegneria “Enzo Ferrari,” Università degli Studi di Modena e Reggio Emilia, Via P. Vivarelli 10/1, 41125 Modena (MO), Italy

^{a)}Author to whom correspondence should be addressed: francescomaria.puglisi@unimore.it. Tel.: +39-059-2056320

ABSTRACT

As devices scale closer to the atomic size, a complete understanding of the physical mechanisms involving defects in high- κ dielectrics is essential to improve the performance of electron devices and to mitigate key reliability phenomena, such as Random Telegraph Noise (RTN). In fact, crucial aspects of defects in HfO_2 are still under investigation (e.g., the presence of metastable states and their properties), but it is well known that oxygen vacancies (V^+ s) and oxygen ions (O^0 s) are the most abundant defects in HfO_2 . In this work, we use simulations to gain insights into the RTN that emerges when a constant voltage is applied across a $\text{TiN}/(4\text{ nm})\text{HfO}_2/\text{TiN}$ stack. Signals exhibit different RTN properties over bias and, thus, appear to originate from different traps. Yet, we demonstrate that they can be instead promoted by the same O^0 s which change their capture (τ_c) and emission (τ_e) time constants with the applied bias, which, in turn, changes the extent of their electrostatic interactions with the traps that assist charge transport (V^+ s). For a certain bias, RTN is given by the modulation of the trap-assisted current at V^+ s induced by trapping/detrapping events at O^0 s, which are, in turn, influenced by the bias itself and by trapped charge at nearby O^0 s. In this work, we demonstrate that accounting for the effect of trapped charge is essential to provide accurate estimation of the RTN parameters, which allow us to retrieve information about traps and to explain key mechanisms behind complex RTN signals.

Published under an exclusive license by AIP Publishing. <https://doi.org/10.1063/5.0137245>

I. INTRODUCTION

In the era of aggressive scaling, the support of physics-based 3D simulations is becoming more and more fundamental to fully explain the measurement data of electron devices. In fact, the implementation of high- κ materials to replace silicon oxide (e.g., HfO_2)¹ further exacerbated the reliability threats associated with electrically active defects in ultra-thin dielectrics. From this perspective, the understanding of the physical mechanisms ruling over such phenomena is still incomplete, yet essential to possibly overcome the associated reliability threat.² Specifically, due to the higher bulk defect density compared to silicon oxide,¹ HfO_2 exhibits stronger and more complex Random Telegraph Noise (RTN), well known to be one of the most degrading effects in ultra-thin dielectrics that results from trapping/detrapping into/from traps.³ A more refined comprehension of this phenomenon would also be beneficial for emerging applications that exploit its intrinsic

stochastic nature as the entropy source, such as True Random Number Generators (TRNGs).^{4–6} As confirmed by the density functional theory (DFT),⁷ *ab initio*,⁸ and multi-scale modeling studies^{9,10} on HfO_2 -based devices, oxygen vacancies (V^+ s) are the defects most involved in trap-assisted charge transport, while oxygen ions (O^0 s) locally distort the electric field at neighboring V^+ s modulating the overall leakage current and promoting RTN.^{11,12} In fact, both simple (e.g., two-level) and more complex (multi-level, anomalous, temporary, and coupled) RTN signals can be associated with trapping/detrapping mechanisms at O^0 s.¹² In the literature, the analysis of RTN parameters extracted from measured data [e.g., current amplitude (ΔI), capture (τ_c), and emission (τ_e) time constants] is commonly used to retrieve important information about the defects involved, such as their vertical position in the dielectric and/or their typology/physical nature.^{13,14} The RTN parameters of each defect are typically extracted from the Markov

chain that represents such defect, commonly retrieved from the raw signal by using different techniques (e.g., edge-detection,¹⁵ time-lag plots,¹⁶ factorial hidden Markov model¹⁷). Nevertheless, possible interdependencies between different Markov chains are never considered within the RTN parameters extraction procedure, thus neglecting possible defects in electrostatic interactions. By implementing kinetic Monte Carlo (kMC) simulations, we demonstrate the importance of considering mutual electrostatic interdependencies between traps in the evaluation of the defects' RTN parameters. Also, we show that complex RTN signals which show deep alteration of their properties with the applied bias (i.e., so much to be typically assumed to be promoted by different defects) can originate from the same ensemble of defects, which interact differently with each other depending on the local electric field. In fact, the latter is given by the overlap of the applied voltage (V_{APP}) and the (often neglected) contribution of the charge trapped at defect sites, which is instead shown to play a dominant role, especially for low applied bias.¹⁸

II. DEVICES AND SIMULATIONS

We simulated RTN in a Metal–Insulator–Metal (MIM) structure having TiN electrodes and a 4 nm thick HfO_2 (EOT ≈ 0.74 nm) as dielectric materials [Fig. 1(a)]. In order to clearly evaluate the dynamics of the charge trapped at defects at the nanoscale including the effect of their possible mutual electrostatic interactions at different biases and over time, we analyzed a device having an area of 25 nm^2 with the aim of limiting the total number of defects, thus the overall computational burden. By using Ginestra[®] device simulation software,¹⁹ kinetic Monte Carlo (kMC) 3D simulations were implemented to properly consider the stochastic nature of charge trapping and, therefore, RTN.²⁰ In all simulations, we included all the key physical mechanisms occurring in a dielectric, as sketched in Fig. 1(b). Specifically, we included Schottky/thermionic emission (SE), direct tunneling (DT), Fowler–

Nordheim tunneling (FN), band-to-band tunneling (BTBT), drift/diffusion in conduction and valence bands (DD), and non-radiative multi-phonon trap-assisted (MPTAT) tunneling, including all possible charge transitions, i.e., capture/emission from/to top (TE) and bottom (BE) electrode, conduction (CB), and valence (VB) band, other defects (TT—trap-to-trap contribution is considered). For a given defect distribution, the MPTAT model implemented in Ginestra[®] calculates the current flowing through the dielectric considering the process reported in Ref. 24 and according to the electron capture and emission rates of the given defect. The capture time constant of a given trap is defined as $\tau_c = \sum_m \tau_{c,m}$, with m being the number of phonons involved in the MPTAT. Thus, the rate^{8,22,23} is written as

$$\frac{1}{\tau_{c,m}} = N_{source}(E_m) f_{source}(E_m) C_m P_T(E_{source}, E_m), \quad (1)$$

where N_{source} is the density of states at the charge carrier source (e.g., an electrode, conduction or valence band of the material, and another defect). f_{source} indicates the Fermi–Dirac distribution at the charge carrier source, P_T is the electron tunneling probability, and C_m is the multiphonon capture probability, which is defined as

$$C_m = C_0 L(m), \quad (2)$$

where C_0 is a constant and $L(m)$ is the multiphonon transition probability²⁵ and its expression (within the effective-frequency approximation^{26,27}) is

$$L(m) = \left(\frac{f_B + 1}{f_B}\right)^{\frac{m}{2}} \exp(-S(2f_B + 1)) I_m(2S\sqrt{f_B(f_B + 1)}), \quad (3)$$

where S is the Huang–Rhys factor, I_m is the modified Bessel function of order m , and f_B is the Bose–Einstein distribution function.

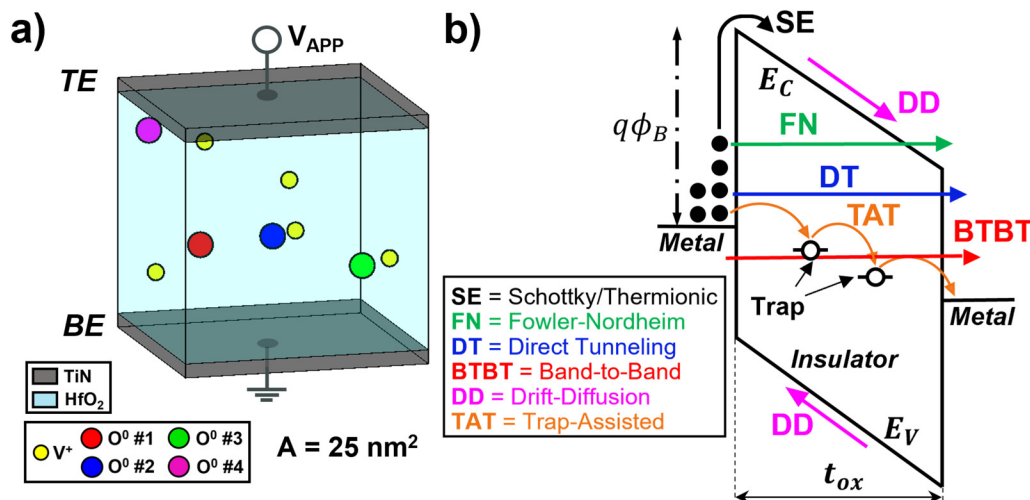


FIG. 1. Representation of (a) the simulated MIM and (b) the main conduction mechanisms involved in the HfO_2 layer and considered in this work.

Downloaded from http://pubs.aip.org/jap/article-pdf/doi/10.1063/5.0137245/16789183/1.14101.1_online.pdf

TABLE I. Main defects and materials parameters used in simulations.

Symbol	Description	V ⁺	O ⁰	HfO ₂
δ _T	Density	5 × 10 ⁻¹⁹ cm ⁻³	4 × 10 ⁻¹⁹ cm ⁻³	...
E _{TH}	Thermal ionization energy	2.2 ± 0.5 eV	2.3 ± 0.5 eV	...
E _{REL}	Relaxation energy	1.2 eV	2.65 eV	...
Σ	Capture cross section	10 ¹⁴ cm ⁻²	3 × 10 ¹⁶ cm ⁻²	...
ħω _{eff}	Phonon energy	0.06 eV	0.06 eV	...
k	Relative dielectric constant	21
k _{TH}	Thermal conductivity	5 × 10 ⁻³ W/cm K
E _G	Bandgap	5.8 eV

Since the capture time depends on the charge carrier source under consideration, and since the latter can, in principle, be TE, BE, CB, VB, or TT, it is necessary to separately calculate each associated capture time. The effective capture dynamics at each defect can then be obtained by considering the inverse capture time in terms of capture probability. The capture time as observed in typical RTN measurements, τ_{c,eff}, can be calculated according to Matthiessen's rule as follows:

$$\frac{1}{\tau_{c,eff}} = \frac{1}{\tau_{c,TE}} + \frac{1}{\tau_{c,BE}} + \frac{1}{\tau_{c,CB}} + \frac{1}{\tau_{c,VB}} + \frac{1}{\tau_{c,TT}} \quad (4)$$

Similar equations to (1)–(4) are adopted also for the emission process,²⁸ replacing the charge carrier source with the charge carrier destination. S is a specific characteristic of each defect species and is related to an important parameter, i.e., the relaxation energy (E_{REL}), by means of the expression E_{REL} = Sħω_{eff}, since it is assumed that localized defect states couple to a single effective vibrational mode with an effective angular frequency ω_{eff}.²⁶ Another key defect property is the thermal ionization energy (E_{TH}), which represents the energy required to remove an electron from the defect and place it in the conduction band. The values of E_{REL} and E_{TH} are typically calculated for each defect species and charge state transition via DFT simulations.^{29,30} In our device [Fig. 1(a)], oxygen vacancies (V⁺s, i.e., oxygen vacancies that are positively charged when empty and neutral upon e⁻ trapping) have E_{REL} = 1.2 eV and E_{TH} = 2.2 ± 0.5 eV, while oxygen ions (O⁰s, i.e., oxygen ions that are neutral when empty and negatively charged upon e⁻ trapping) are characterized by E_{REL} = 2.65 eV and E_{TH} = 2.3 ± 0.5 eV, consistently with earlier DFT reports³¹ and recent multi-scale simulation studies from different research groups.^{9,10} Although oxygen vacancies in HfO₂ may be found in five different charge states (V²⁺, V⁺, V⁰, V⁻, V²⁻) and oxygen ions in three charge states (O⁰, O⁻, O²⁻),²⁹ for simplicity and with no loss of generality, here, we only consider the most relevant charge transitions (i.e., V⁺ ↔ V⁰ and O⁰ ↔ O⁻). For completeness, all the main defects and materials parameters used in the simulation are reported in Table I. Most importantly, the full 3D Poisson equation is solved explicitly including the trapped charge term to completely account for electrostatic interactions in the dielectric due to the trapped charge³² and to consider its effect on the local 3D potential profile as well as on the tunneling barriers for SE, DT, BTBT, and TAT. Importantly, as depicted in Fig. 2(a), we verified that in the

whole range of V_{APP} (0.45–0.75 V), the leakage current through the stack is dominated by TAT at V⁺s. Specifically, we adopted such an applied bias range since it generates electric field values within the oxide, which correspond to those typically observed in the gate stack of transistors and memory-devices (e.g., RRAMs) in operating conditions.³³ In addition, according to the IEEE International Roadmap for Devices and Systems (IRDS),³⁴ these V_{APP} match the forecast scaling V_{DD} for the next-generation devices for logic circuits. On the contrary, as discussed in our previous work,¹⁸ for thinner oxide layers the leakage current might be dominated by direct tunneling (DT) rather than by trap-assisted tunneling (TAT) at V⁺s. Therefore, RTN can result from the effect of the E-field perturbation given by trapped charge at O⁰s on DT barriers seen by e⁻ at the injecting electrode, but the same framework and

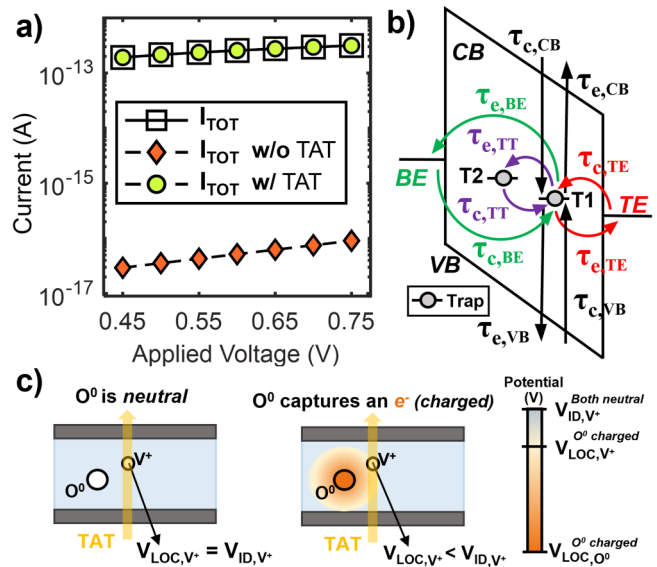


FIG. 2. (a) Analysis of the conduction mechanisms involved in the HfO₂ layer (TAT is dominant). (b) Representation of e⁻ capture and emission processes, which can occur for a single trap in the oxide (T1) from all possible sources and to all possible destinations. (c) Illustration of TAT current modulation induced by capture/emission activities at O⁰s, which change the local potential value at the V⁺s involved in the charge transport.

Downloaded from http://pubs.aip.org/jap/article-pdf/doi/10.1063/5.0137245/16788183/114101_1_online.pdf

considerations remain valid. In our structure [Fig. 1(a)], we considered bi-state V^+ s ($N_V^+ = 5 \times 10^{19} \text{ cm}^{-3}$) and O^0 s ($N_O^0 = 4 \times 10^{19} \text{ cm}^{-3}$). These density values are in-line with the values used in earlier reports to simulate the behavior of unstressed HfO_2 devices.³⁵ V^+ s are positively charged when empty and neutral when they capture an e^- , while O^0 s are neutral when empty and negatively charged when filled by an e^- . Oxygen vacancies have been identified as the defects most involved in defect-assisted charge transport,^{29,30} though oxygen ions have shown to play a crucial role in resistive switching and in determining RTN in HfO_2 .^{11,12} As depicted in Fig. 2(b), for each defect, the simulator calculates the capture (τ_c) and emission (τ_e) time constants for each possible charge source/destination, since each trap can capture/emit charge carriers from/to the TE, BE, TT, VB, and CB. Moreover, since kMC transient simulations specifically include the carriers trapping kinetic (i.e., each trapping and detrapping event is actually simulated and not just described by means of an event probability), it is possible to extract the charge state (i.e., if the defect is empty or full and its occupancy probability), as well as the local potential value, for each V_{APP} and at each instant of time. Since V^+ s are characterized by lower relaxation energy compared to O^0 s, the former are commonly defined as *fast* traps since they are faster in capturing/emitting charge carriers and thus able to conduct a significant amount of current through the dielectric. Conversely, the latter are defined as *slow* traps and do not significantly contribute to charge transport. In fact, since the defect time constants are directly proportional to the exponential of the Huang–Rohys factor, S (i.e., directly related to the relaxation energy^{27,36}), the lower the relaxation energy the lower the capture (emission) time constant (and consequently the faster the defect). In Fig. 2(c), we depicted how the RTN can emerge from an O^0 s-induced modulation of the leakage current driven by V^+ s. In fact, when an ion captures an electron (becoming negatively charged), the trapped charge at such O^0 alters the local potential at the V^+ s in its vicinity, which decreases as compared to the ideal value (V_{ID} , i.e., the local potential if the effect of the trapped charge is not considered). This abrupt change in the local potential reflects in a change in the V^+ s capture and emission times, thus in the TAT current they drive. Upon the emission of charge from the ion, the previous value of the local potential at the V^+ s is restored, which also restores the TAT current to its previous value. This dynamic occurs for each O^0 s (which also interact in the same way with nearby O^0 s and not only with V^+ s), promoting a complex time-dependent multibody problem within the oxide, which results in the observed RTN.

To grasp the activity of O^0 s and its effect on RTN as detected in experiments, it is necessary to adopt tailored sampling (t_{sam}) and simulation (t_{sim}) times for each V_{APP} . In fact, only the O^0 s that have sufficiently balanced capture (τ_c) and emission (τ_e) time constants can result in RTN that can be properly detected in experiments (i.e., traps showing a τ_c/τ_e ratio between 10^{-2} and 10^2 , approximately). This lets us avoid under- or over-sampling (that are very critical aspects in RTN measurement and analysis³⁷) at each V_{APP} , which may distort the RTN signal. For a given V_{APP} , to completely detect the trapping activity of O^0 s (and thus the possible RTN phenomena), it is necessary to choose a sampling time (t_{sam}) lower than the O^0 s capture/emission time constants and a much longer simulation time (t_{sim}), namely, meeting the following

criterion: $t_{\text{sam}} < \tau_{c,e} < t_{\text{sim}}$.³⁷ Nevertheless, since the τ_c and τ_e of defects change with the applied bias, we adjusted t_{sam} and t_{sim} accordingly for each V_{APP} . Specifically, at 0.45 V, we adopted $t_{\text{sam}} = 0.4$ s and $t_{\text{sim}} = 8 \times 10^3$ s; in the range 0.50–0.60 V, we choose $t_{\text{sam}} = 0.2$ s and $t_{\text{sim}} = 4 \times 10^3$ s; and in the range 0.65–0.75 V, we considered $t_{\text{sam}} = 0.1$ s and $t_{\text{sim}} = 2 \times 10^3$ s. Each trace is composed by 2×10^4 equally spaced simulated points.

III. RANDOM TELEGRAPH NOISE ANALYSIS

As depicted in Fig. 3(a), in our device 5 V^+ s and 4 O^0 s are present within the HfO_2 layer. However, we verified that at each V_{APP} there is a primary V^+ [highlighted in the bulk of the oxide in Fig. 3(a)], which drives the largest share of current by TAT, and two main O^0 s [namely, the #1 (red) and #2 (blue)] which modulate such current over time by trapping and detrapping charge. Precisely, V^+ emphasized in Fig. 3(a) results being the one mostly involved in TAT due to its central position in space (i.e., it is located in the middle of the HfO_2 thickness) and energy (i.e., the V^+ is energetically aligned to the Fermi level of the electrodes, allowing both e^- capture and emission processes at such traps and thus contributing to the leakage). In fact, at each V_{APP} , O^0 s #3 (green) and #4 (magenta) are always neutral (empty) due to their position in energy and space, having $\tau_c \gg \tau_e \gg t_{\text{sim}}$. Therefore, their effect (i.e., their trapping activity) is not appreciable within the simulated RTN signal. As there are two bi-state O^0 s, which promote such signals (namely, #1 and #2), $2^2 = 4$ possible O^0 s charge configurations can occur [that we labeled A, B, C, and D, Fig. 3(b)], each determining a unique 3D potential profile in the dielectric and, therefore, a unique value of the local electric field at the V^+ , which is mainly involved in TAT [Fig. 3(a)], in turn, associated with a unique current level. Notably, configuration A is characterized by O^0 #1 and #2 both charged (full), while D represents the case in which all O^0 s are neutral (empty). As defined in Sec. II,

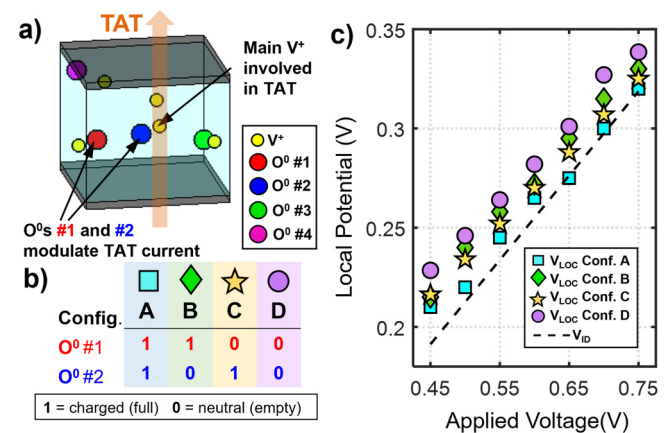


FIG. 3. (a) Visualization of the V^+ , which assists the current and of the O^0 s, which are responsible for RTN. (b) Representation of the four possible O^0 s configurations. (c) Comparison of the local potential values at the V^+ highlighted in (a), at each V_{APP} and for each O^0 s configuration, compared to the ideal local potential (V_{ID}) at such V^+ .

the ideal potential (V_{ID}) within the HfO_2 is the potential value (for a specific Z coordinate, since we apply a constant bias at the TE) if the trapped charge is not considered, i.e., all defects are neutral, and they do not alter the linear potential profile along the Z coordinate within the oxide. Since V^+ s become neutral once they capture an e^- , and they are positively charged when they emit an e^- , trapped charge at V^+ s can increase the local potential within the oxide (which becomes greater compared to the V_{ID}). On the contrary, since O^0 s are neutral when empty and negatively charged once filled by an e^- , O^0 s can provide a negative charge within the HfO_2 , in turn, lowering the local potential compared to the ideal one (V_{ID}). Therefore, at the time instant in which configuration D occurs (i.e., all O^0 s are neutral), the potential within the oxide cannot be locally reduced but only increased by the trapped charge at V^+ s. In Fig. 3(c), for each V_{APP} and for each O^0 s configuration, we reported the local potential at the V^+ highlighted in Fig. 3(a). Obviously, in the whole range of V_{APP} , configuration D is associated with higher local potential values compared to the other configurations, while the lower local values are obtained when configuration A occurs, which brings the potential close to the ideal potential value at the V^+ (V_{ID} , dashed line). However, as can be seen in Fig. 3(c), the local potential at the V^+ is always \geq to the V_{ID} , since (i) within the oxide the number of V^+ s (5) is $>$ than the number of O^0 s (4), (ii) V^+ s nearby to the V^+ of interest are positively charged, and (iii) 2 out of 4 O^0 s (namely, #3 and #4) are always neutral and therefore they do not provide negative charge (i.e., a local potential reduction at the V^+). As we highlighted in our previous works,^{18,32} the local potential within the oxide is given by the overlap of the applied voltage and the possible contribution of trapped charge. Notably, the local potential varies dynamically since (in contrast to the V_{APP} , which is kept constant over time in this study) the trapped charge contribution is given by the specific O^0 s configuration, which changes over time and with the applied voltage. In Fig. 4, we depicted the simulated RTN traces at different V_{APP} . For each signal, each individual current level is associated with a unique O^0 s configuration. Also, the simulator allows extracting the Markov chain of each O^0 (even if only the ones of O^0 #1 and #2 matter), and we depicted examples of such chains for specific chunks of RTN on the right of each panel in Figs. 4(a)–4(g). As evidenced, the O^0 s Markov chains represent the evolution of the O^0 s configurations [Fig. 3(b)] in the time domain, and their overlapped effect at each instant of time determines the current level of the RTN. As highlighted in Fig. 4(g), the current levels are characterized by the typical white noise, which emerges from the inherent stochastic features of the V^+ -assisted charge transport [Fig. 3(a)]. For a specific V_{APP} [Figs. 4(a)–4(g)], the RTN signal is given by the modulation of the TAT, which reflects the evolution in the time domain of the trapping/detrapping events at O^0 #1 and #2 (i.e., such O^0 s Markov chains), which dynamically and simultaneously change the local potential value at the V^+ shifting the current in specific levels. Notably, for $V_{APP} \leq 0.65$ V [Figs. 4(a)–4(e)], we observe a four-level RTN, namely, the TAT modulation promoted by both O^0 #1 (red) and #2 (blue), since the activity of O^0 #2 is appreciable both when #1 is full (i.e., its Markov chain is equal to 1) and when is empty. Nevertheless, in such a V_{APP} range (0.45–0.65 V), it can be seen that the RTN current amplitude promoted by O^0 #2 (blue) increases with V_{APP} when O^0

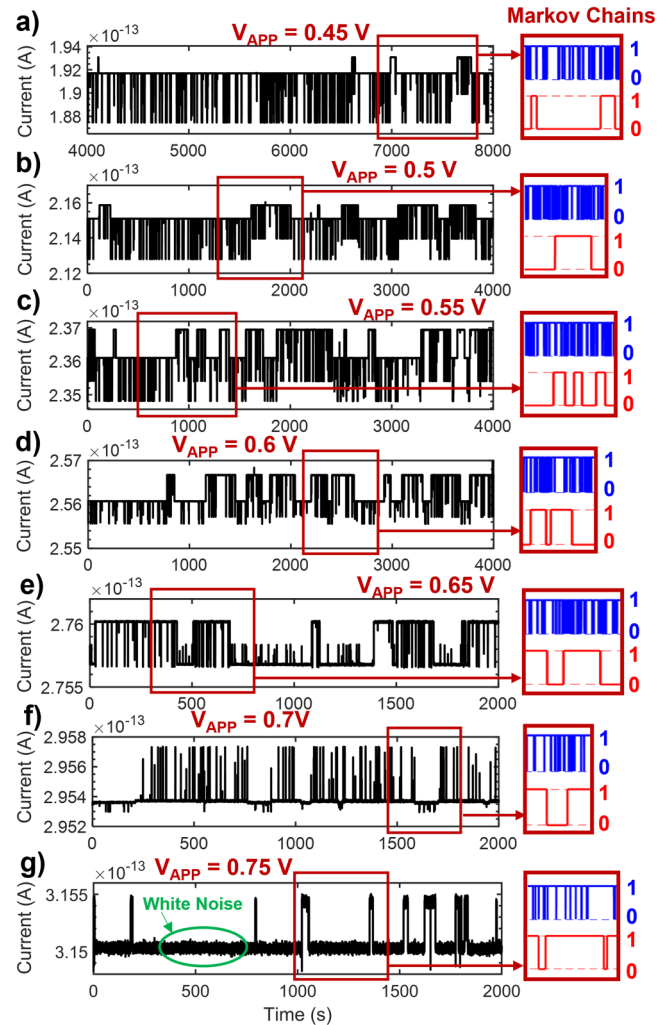


FIG. 4. (a)–(g) RTN traces at different V_{APP} (0.45–0.75 V). On the right, chunks of Markov chains of O^0 #1 and #2 are highlighted for each RTN signal.

#1 (red) is charged (i.e., its Markov chain is at 1) and decreases with V_{APP} when O^0 #1 is neutral (i.e., its Markov chain is at 0). Interestingly, it can be noted that for $V_{APP} \leq 0.7$ V, the current level decreases when O^0 #1 (red) gets empty and increases when it captures an e^- , reflecting the Markov chain of O^0 #1. On the contrary, at 0.75 V [Fig. 4(g)], the current has the opposite behavior than the Markov chain of O^0 #1, being higher when the defect is empty and lower when it gets charged. Also, at 0.7 V [Fig. 4(f)] the signal is more similar to a two-level RTN since the activity of O^0 #2 is not much appreciable when #1 is empty. Downright, even if still given by the overlap of the same Markov chains, a well-established two-level RTN even appears at 0.75 V [Fig. 4(g)], giving the feeling that the activity of O^0 #2 is almost completely buried in the white noise.

As well known, the analysis of an RTN signal³⁷ includes the evaluation of three main parameters, such as the current amplitude

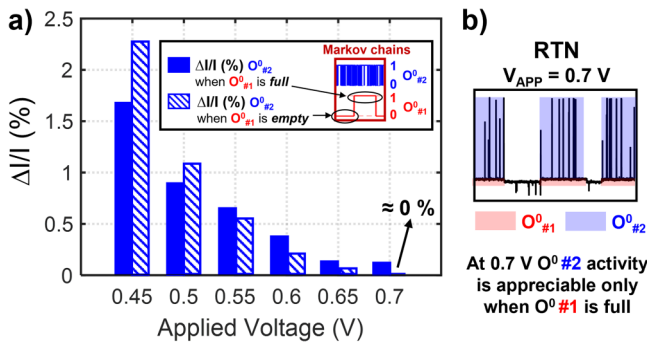


FIG. 5. (a) Analysis of the amplitude percentage variations $[\Delta I/I$ (%) of the RTN given by O^0 #2 depending on the charge state of O^0 #1. (b) Peculiar RTN chunk at 0.7 V given by the effect of different configurations of the O^0 s, which (differently) modulate TAT.

between two levels (ΔI), and the capture (τ_c) and emission (τ_e) time constants, which characterize each Markov chain involved in the process. Thus, in Subsections III A and III B, we perform an accurate quantitative analysis of these parameters to highlight the importance of considering the electrostatic interdependencies between defects and their effect on the overall RTN.

A. Current amplitudes (ΔI)

As discussed previously, we can see how the RTN amplitudes between the current levels, which characterize each signal [Figs. 4(a)–4(g)] change over V_{APP} , giving the impression that there are no correlations between the defects which promote such RTN traces. In Fig. 5(a), for each V_{APP} , we analyzed the amplitude percentage variations $[\Delta I/I$ (%) of O^0 #2 when O^0 #1 is full (charged)

and when it gets empty (neutral), as depicted within the inset. As already highlighted, we can quantitatively appreciate how the $\Delta I/I$ % of O^0 #2 varies when the #1 is full or empty, as well as when V_{APP} changes. Moreover, at 0.7 V, the RTN signal seems to have only two levels, being the activity of O^0 #2 almost not perceptible when #1 is empty compared with the case in which #1 holds an electron. In fact, the analysis of Fig. 5(a) reveals that the $\Delta I/I$ value of #2 is approximately 0%. Without the support of the Markov chains [Figs. 4(a)–4(g), right panels], the RTN signals can be related to various phenomena due to the different RTN parameters that characterize each signal,⁴¹ such as the presence of different defects, the existence of metastable states of defects,^{38–40} and/or traps which activate each other,⁴¹ depending on the V_{APP} . Indeed, Grill *et al.*⁴¹ highlighted a peculiar RTN in which a trap can be activated by the trapped charge at another trap, resulting in a signal comparable to the one at 0.7 V [Fig. 5(b)], which seems to be originated by the same mechanism. In fact, the activity of O^0 #2 is appreciable only when O^0 #1 is full and is almost 0% when #1 gets empty [Fig. 5(a)]. Nevertheless, as clarified by the Markov chains of Fig. 4(f), the Markov chain of O^0 #2 (blue) does not show particular changes over the one of #1 (red), meaning that #1 does not activate/deactivate #2 by trapping/detrapping charge. Indeed, the peculiar RTN at 0.7 V emerges as a consequence of the different local potential conditions induced at the V^+ which drives current differently according to the evolution of the O^0 s configurations. Therefore, complicated RTN mechanisms are not necessarily associated with complex phenomena, but they can arise from simple mechanisms (i.e., Markov chains) that interact dynamically with each other and with the surrounding landscape (for a given V_{APP}), thus generating complexity.

B. Capture (τ_c) and emission (τ_e) time constants

In Fig. 6(a), we depicted the ratio of the time constants (τ_c/τ_e) vs V_{APP} of O^0 #1 and #2, since it is a typical way of reporting the

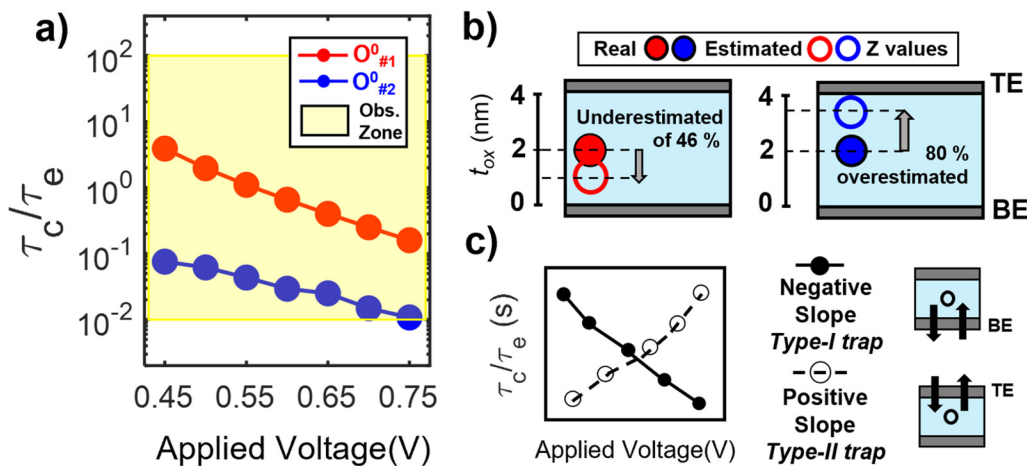


FIG. 6. (a) τ_c/τ_e vs V_{APP} for O^0 #1 (red) and #2 (blue). The observable zone (yellow area) highlights the range in which τ_c and τ_e have values that can be detected in typical electrical measurements. (b) Comparison between the real O^0 #1 and #2 vertical positions and those estimated by using the formula proposed in Ref. 13. (c) Defect's τ_c/τ_e slope-based classification according to Ref. 13.

Downloaded from http://pubs.aip.org/jap/article-pdf/doi/10.1063/5.0137245/16789183/1.14101.1_online.pdf

characteristics of defects involved in RTN. In fact, in the literature, the τ_c/τ_e trends of defects vs applied bias are quite revealing, as they are commonly used to evaluate the defects' vertical position in the oxide and/or to provide a traps' classification.^{13,14} Generally, for a given V_{APP} , the τ_c and τ_e values associated with a single defect are directly extracted from its Markov chain (which can be obtained by decomposing the overall RTN signal via different post-processing techniques, e.g., FHMM¹⁷) and then averaged over time, thus considering τ_c and τ_e as expected values of respective exponential distributions.³⁸ To mimic this "conventional" approach, we extracted in the time domain the τ_c and τ_e values of each defect (only O^0 #1 and #2 are of interest) obtaining five different τ_c and τ_e values for each instant of time. Specifically, five values are obtained since a single defect can capture/emit from/to the bottom electrode (BE), top electrode (TE), other traps (TT), valence (VB), and conduction (CB) bands. However, for each instant of time, only the lowest τ_c (τ_e) value is the most relevant, i.e., the most likely source (destination), and this is accounted for by averaging τ_c (τ_e) over all possible sources (destinations) by using Matthiessen's rule (4). Thus, the effective τ_c and τ_e are averaged (as the average of exponential distributions) over time, obtaining the same dwell times that would have been commonly extracted from measurements, and the relative τ_c/τ_e trends vs V_{APP} are those in Fig. 6(a). The yellow zone highlights τ_c and τ_e values that are easily accessible by experiments (i.e., the observable zone): in our simulations, they identify the defects which cause RTN that is visible within the adopted observation window (see Sec. II). As expected, only O^0 #1 and #2 have τ_c/τ_e , which belong to the observable zone, while O^0 #3 and #4 have $\tau_c \gg \tau_e \gg t_{sim}$ (not shown) for each V_{APP} and, therefore, do not give any contribution to the RTN signals under investigation (Fig. 4). Since both τ_c/τ_e vs V_{APP} exhibit monotonic trends with a negative slope, in Fig. 6(b), we estimated their vertical position within the dielectric by using the formula reported in Ref. 13. As can be seen, O^0 #1 position is 46% underestimated and #2's is 80% overestimated compared to their actual Z coordinate, meaning that the formula is oversimplified and/or such τ_c and τ_e values are not sufficiently reliable for this analysis. Furthermore, according to the defect-type classification reported in Ref. 13 [Fig. 6(c)], O^0 #1 and

#2 should be classified as type-I traps (i.e., defects which exchange charge only with the BE), since both O^0 's exhibit a monotonic negative τ_c/τ_e slope [Fig. 6(a)]. However, in the following analysis, we demonstrate that such classification is not reliable, since it is based on the idea that the capture and emission time constants of a single defect can be extracted directly from its Markov chain without accounting for the impact of nearby traps. In fact, it is not considered that the τ_c (τ_e) value of a defect can be different if a nearby defect is neutral or charged, even if the trapped charge for RTN phenomena has been shown to have great relevance.³² Basically, trapping dynamics at one defect can be affected stochastically by the one at a nearby defect and vice versa, since (i) trapped charge at the latter can modify the local potential profile at the former (also depending on the applied voltage value) and (ii) the availability of states of the latter (namely, the actual possibility for such a trap to accommodate an e^-) changes accordingly, making some capture/emission processes more likely than others for specific instants of times. Therefore, to provide better accuracy in evaluating the τ_c and τ_e of each defect (and, therefore, the overall RTN characteristics), we cannot assume that there is only one distribution for the capture (emission) process, but there are as many τ_c (τ_e) distributions as many charge states of the defects involved in RTN. In this case, having two bi-state defects, which contribute to the RTN (namely, O^0 #1 and #2, since the #3 and #4 are always neutral), we evaluated the τ_c of O^0 #1 when the #2 is full [$\tau_{c1,2(full)}$ —red circle] and when #2 gets empty [$\tau_{c1,2(empty)}$ —empty rhombus], obtaining two different capture time constant trends over V_{APP} [Fig. 7(a)]. Obviously, since we are evaluating the capture process, the τ_c values are always estimated considering the instants of time in which the #1 is empty (i.e., it makes no sense to evaluate τ_c of a defect when it is full since it cannot host any e^-). Similarly, in Fig. 7(b), we evaluated the emission time constants for #1 when #2 is neutral [$\tau_{e1,2(empty)}$ —red circle] and when it holds an e^- [$\tau_{e1,2(full)}$ —empty rhombus], in both cases, considering the instants of time in which #1 is full (i.e., it makes no sense to evaluate τ_e of a defect which does not host e^- that can be emitted). Also, we reported $\tau_{c,1}$ [Fig. 7(a)] and $\tau_{e,1}$ [Fig. 7(b)], namely, the capture and emission time constants extracted by the "conventional"

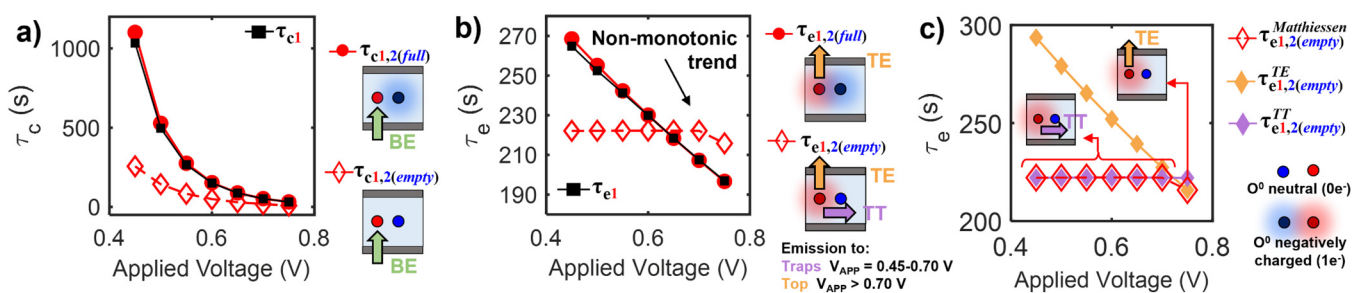


FIG. 7. Analysis of the capture (a) and emission (b) time constant trends vs V_{APP} for O^0 #1 (red defect in the sketches). For both capture and emission processes, three different trends are reported, namely, the one considering the nearby O^0 #2 (blue defect in the sketches) negatively charged [$\tau_{c1,2(full)}$ and $\tau_{e1,2(full)}$ —filled red circles] and neutral [$\tau_{c1,2(empty)}$ and $\tau_{e1,2(empty)}$ —empty red rhombuses] and also the one obtained by using the "conventional" approach (τ_{c1} and τ_{e1} —black squares), which corresponds to what would be extracted from experiments. (c) Analysis of the non-monotonic trend observed in (b), which is given by a change in the more likely emission destination with V_{APP} .

approach (i.e., without separately considering the possibility for O^0 #2 to be empty or full), for each V_{APP} . For both capture [Fig. 7(a)] and emission [Fig. 7(b)] processes, such trends (black squares) are circumscribed by the two distributions which are related to the two different possible charge states of O^0 #2 (namely, the red circles and empty rhombus) but still very close to the distribution obtained considering the #2 full (red circles). In fact, this was to be expected since as can be inferred from the Markov chains in Figs. 4(a)–4(g), O^0 #2 defect is almost always negatively charged (full). Interestingly, even if statistically less likely, when O^0 #2 gets neutral the trend $\tau_{e1,2(\text{empty})}$ [Fig. 7(b)—empty rhombus] is very different from the one in which #2 is full [$\tau_{e1,2(\text{full})}$ —red circles], the former also exhibiting a non-monotonic behavior with a (mild) positive slope between $V_{APP} = 0.45$ – 0.7 V and a negative slope for $V_{APP} > 0.7$ V. Our previous works^{18,32} revealed that non-monotonic τ_c/τ_e trends vs V_{APP} can be related to changes in capture source and/or emission destination of defects, demonstrating that the slope of such time constant trends cannot be unambiguously used to provide a reliable defect classification. In fact, in Fig. 6(c), we reported the traps' classification used in Refs. 13 and 14 according to which O^0 #1 and #2 should be classified as type-I traps (i.e., exchanging charge only with BE). However, as can be seen in the stack representations of Figs. 7 and 8, both #1 and #2 capture charge from the BE and emit charge to the TE, disagreeing with the classification of Fig. 6(c).^{13,14} Also, we verified that O^0 #1 changes emission destination over V_{APP} , emitting toward other

traps in the range of $V_{APP} = 0.45$ – 0.7 V and at the TE for $V_{APP} > 0.7$ V, in agreement with our recent findings.^{18,32} Since the $\tau_{e1,2(\text{empty})}$ trend has been evaluated by using Matthiessen's rule (4), i.e., considering that the trap can emit to 5 possible destinations (namely, TE, BE, TT, VB, and CB), we evaluated the emission time constants associated with each destination (but only the one associated with the emission to the TT and TE matter), and the results are reported in Fig. 7(c) for each V_{APP} . As can be seen, the $\tau_{e1,2(\text{empty})}$ trend results from the fact that the most probable process changes over V_{APP} , since the distribution associated with emission to traps (TT) and with the TE cross each other in between 0.7 and 0.75 V. In Fig. 8, we reported the same analysis made for #1 (Fig. 7) for O^0 #2. As can be seen, capture [Fig. 8(a)] and emission [Fig. 8(b)] time constant distributions are quite similar to each other, both qualitatively (since the trends associated with different #1 charge states possess the same behavior) and quantitatively. Still, the capture [$\tau_{c,2}$ —Fig. 8(a)] and emission [$\tau_{e,2}$ —Fig. 8(b)] time constants extracted by the "conventional" approach possess intermediate values between the two distributions which account for the charge state of O^0 #1 (namely, the blue circles and empty rhombuses).

Unlike #1, O^0 #2 does not exhibit non-monotonic trends, and it captures charge from the BE and emits charge to the TE at each V_{APP} . To understand the physical reason behind this difference, in Fig. 9, we analyzed for #1 [Fig. 9(b)] and #2 [Fig. 9(c)], the local potential value at each V_{APP} . Here, we reported the ideal potential, V_{ID} , values [Figs. 9(b) and 9(c)—black square] for both defects, i.e., the potential at the defects (for a given V_{APP}) if the effect of trapped charge on the electric field within the oxide is not considered at all. Notably, since such O^0 s are located at the same Z coordinate = 2 nm [Fig. 9(a)—side view], they possess the same V_{ID} for each V_{APP} . In Fig. 9(b), it is possible to appreciate the impact of the trapped charge at #2 on the O^0 #1 over V_{APP} . In fact, when #2 traps an e^- , the local potential at #1 gets low (filled circle) compared to the case in which #2 is vacant (empty circle). However, in the latter, the local potential at #1 is still lower compared to the ideal value since we are considering #1 itself full (negatively charged) in order to evaluate the local potential values which rule over the emission process. By comparing Figs. 9(b) and 9(c), it is evident that the trapped charge at #2 strongly affects the local potential at #1, while trapped charge at #1 does not perturb the local potential at #2 with the same intensity. This is because the local potential at O^0 #2 is locally increased by the positively charged V^+ , which is located in its vicinity [Fig. 9(a)—top view]. Therefore, the physical reason behind the change in emission destination of #1 with V_{APP} [Figs. 7(b) and 7(c)] is imputable to the amount of the local potential reduction, which is stronger than the one perceived by #2. To evaluate this aspect, we compared the percentage local potential reduction at #1 when #2 is empty [Fig. 9(d)]. Considering #2 empty is necessary to consider the possibility of emission toward all destinations, including other traps (specifically, toward #2). In the opposite case, #2 would have no availability of states and the emission process from #1 to #2 would be impossible. The same analysis is shown in Fig. 9(e) for #2 when #1 is empty. Notably, in the conditions of both Figs. 9(d) and 9(e), defects can emit an e^- toward each other. From such analysis, since the most likely emission destination for #1 changes between $V_{APP} = 0.7$ – 0.75 V, we can

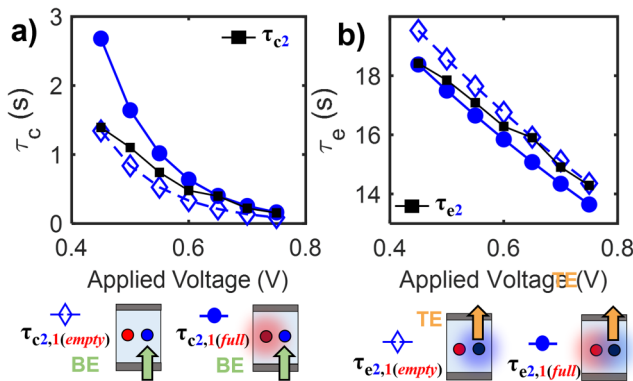
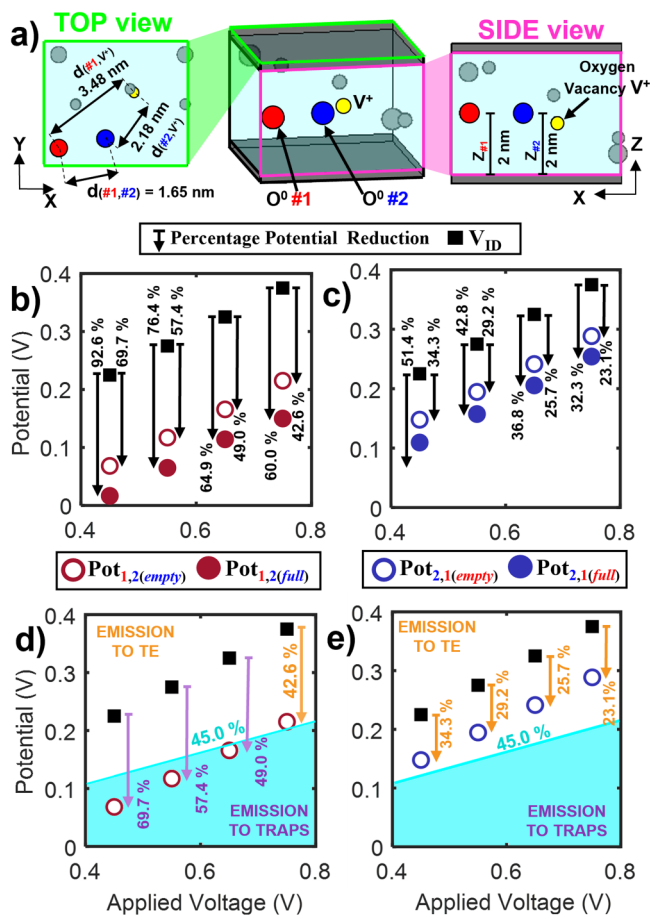


FIG. 8. Analysis of the capture (a) and emission (b) time constant trends vs V_{APP} for O^0 #2 (blue defect in the sketches). For both capture and emission processes, three different trends are reported, namely, the one considering the nearby O^0 #1 (red defect in the sketches) negatively charged [$\tau_{c2,1(\text{full})}$ and $\tau_{e2,1(\text{full})}$ —filled blue circles] and neutral [$\tau_{c2,1(\text{empty})}$ and $\tau_{e2,1(\text{empty})}$ —empty blue rhombuses] and also the one obtained by using the "conventional" approach (τ_{c2} and τ_{e2} —black squares), which corresponds to what would be extracted from experiments. Analysis of the capture time constant distributions for O^0 #2 (blue). Three different distributions are reported, namely, considering mutual interdependencies between Markov chains of defects ($\tau_{c,2}$ —black squares) and considering the nearby O^0 #1 (red) negatively charged [$\tau_{c2,1(\text{full})}$ —blue circles] and neutral [$\tau_{c2,1(\text{empty})}$ —empty rhombus]. (b) Analysis of the emission time constant distributions for O^0 #2. The three different distributions are associated with the same conditions reported in [(a)—same symbols and colors].



infer that a local potential reduction greater than 45% (i.e., that is true in the range $V_{APP} = 0.45\text{--}0.7\text{ V}$) is likely to encourage the emission to other traps (TT), while a percentage potential reduction less than 45% (true for $V_{APP} > 0.7\text{ V}$) promotes the emission to the TE. This is in line with the fact that the percentage potential reduction decreases with increasing V_{APP} : at large V_{APP} , the relative effect of the trapped charge on the local potential is milder, while it is dominant at small V_{APP} .¹⁸ Coherently, since the local potential at #2 is reduced less than 45% at each V_{APP} , such trap always emits to the TE.

IV. CONCLUSIONS

In this work, we analyzed the details of the process modulation of the V^+ -assisted TAT current due to charge trapping/detrapping events at O^0 s that results in RTN. The analysis was performed on TiN/(4 nm)HfO₂/TiN cell, where the leakage current is found to be dominated by TAT. By changing the applied voltage ($0.45\text{--}0.75\text{ V}$), we have shown how several multi-level RTN traces characterized by different RTN parameters (ΔI , τ_c , τ_e) can be promoted by the same two O^0 s (i.e., the same couple of Markov chains), which modify each other's local potential (as well as the one at V^+ s) differently depending on the specific applied bias condition. By analyzing the $\Delta I/I$ (%) of one of the two O^0 s involved, we demonstrated that peculiar RTN signals (commonly associated with the presence of more sophisticated phenomena, e.g., the presence of metastable states of defects) can emerge following specific local electric field conditions at the defects, which assist the charge transport. In fact, such behaviors are dictated by the local electric field value which is given by the overlap of the field due to the applied voltage and the (frequently neglected) field contribution due to possible trapped charge within the oxide, which also changes over time (due to trapping and detrapping). Considering the impact of the field perturbation due to trapped charge, we showed that the "conventional" approach adopted to estimate the τ_c and τ_e of defects of experimental RTN traces provides values that are inherently altered by the effect of the trapped charge in the surroundings of the defect under consideration (i.e., at other defects nearby). In fact, the τ_c/τ_e trend of defects, which promote RTN is generally plotted vs V_{APP} to retrieve key defects information (e.g., the vertical position within the oxide), which are here shown to lead to misinterpretations since the retrieved τ_c and τ_e are affected by local potential perturbations due to trapping events at other nearby defects within the oxide.

Results put in the spotlight the role of electrostatic interactions between traps on the RTN characteristics, and how trapped charge can dominate the local potential within the material causing a complex and unpredictable electrostatic scenario. Additional complexity is expected when phenomena like defect drift/diffusion and generation/recombination are considered.⁴² Moreover, further complexity together with even larger potential perturbations by charged defects are expected if the possibility for oxygen ions to host more than one electron is considered,^{29,43} further stressing the importance of the conclusions drawn in this paper. Given that the relative effect of trapped charge on the local electric field is higher at low V_{APP} , the evaluation of such phenomena assumes greater relevance with technological scaling (due to supply voltage reduction) and in ultra-low voltage applications. Therefore, the effects of trapped charge on the local potential are expected to be dominant in next-generation devices and novel transistor architectures (such as fork-sheets and nanowires), which will pose severe challenges in terms of reliability predictions as the local field will be dominated by stochastic and mutually interfering events rather than by the applied voltage. As the opposite, in devices that use a higher supply voltage such effects may be much less important at least in the pristine state, where the defect density may be low enough so as to render mutual defects interactions negligible. However, long term degradation associated with significant defects generation will inevitably

lead to a much stronger relevance of the trapping activity at defects on the local electric field within the oxide, which should be taken into account when analyzing end-of-life reliability and the device lifetime.

ACKNOWLEDGMENTS

The authors acknowledge Applied Materials Italy for their support with Ginestra¹⁹ device simulation software.

AUTHOR DECLARATIONS

Conflict of Interest

The authors have no conflicts to disclose.

Author Contributions

Sara Vecchi: Conceptualization (supporting); Data curation (lead); Formal analysis (lead); Investigation (lead); Methodology (lead); Software (lead); Validation (lead); Visualization (lead); Writing – original draft (lead); Writing – review & editing (equal). **Paolo Pavan:** Conceptualization (supporting); Writing – review & editing (supporting). **Francesco Maria Puglisi:** Conceptualization (lead); Data curation (supporting); Formal analysis (supporting); Funding acquisition (lead); Investigation (equal); Methodology (equal); Project administration (lead); Resources (lead); Software (supporting); Supervision (lead); Validation (supporting); Visualization (supporting); Writing – original draft (supporting); Writing – review & editing (lead).

DATA AVAILABILITY

The data that support the findings of this study are available from the corresponding author upon reasonable request.

REFERENCES

- ¹J. Robertson, “High dielectric constant oxides,” *Eur. Phys. J. Appl. Phys.* **28**, 265–291 (2004).
- ²N. Raghavan *et al.*, “Microscopic origin of random telegraph noise fluctuations in aggressively scaled RRAM and its impact on read disturb variability,” in *IEEE International Reliability Physics Symposium Proceedings* (IEEE, 2013), pp.1–7.
- ³D. Veksler *et al.*, “Random telegraph noise (RTN) in scaled RRAM devices,” in *IEEE International Reliability Physics Symposium Proceedings* (IEEE, 2013), pp. 1–4.
- ⁴M. Lanza *et al.*, “Memristive technologies for data storage, computation, encryption, and radio-frequency communication,” *Science* **376**(6597), 1–13 (2022).
- ⁵R. Brederlow, R. Prakash, C. Paulus, and R. Thewes, “A low-power true random number generator using random telegraph noise of single oxide-traps,” in *2006 IEEE International Solid State Circuits Conference—Digest of Technical Papers* (IEEE, 2006), pp. 1666–1675.
- ⁶C. Wen *et al.*, “Advanced data encryption using 2D materials,” *Adv. Mater.* **33**(27), 1–12 (2021).
- ⁷D. Muñoz Ramo, J. L. Gavartin, A. L. Shluger, and G. Bersuker, “Spectroscopic properties of oxygen vacancies in monoclinic HfO₂ calculated with periodic and embedded cluster density functional theory,” *Phys. Rev. B* **75**(20), 1–12 (2007).
- ⁸T. V. Perevalov, and D. R. Islamov, “Atomic and electronic structures of the native defects responsible for the resistive effect in HfO₂: ab initio simulations,” *Microelectronic Engineering* **216**, 111038 (2019).

- ⁹J. Strand, P. La Torraca, A. Padovani, L. Larcher, and A. L. Shluger, “Dielectric breakdown in HfO₂ dielectrics: Using multiscale modeling to identify the critical physical processes involved in oxide degradation,” *J. Appl. Phys.* **131**(23), 234501 (2022).
- ¹⁰A. Padovani, D. Z. Gao, A. L. Shluger, and L. Larcher, “A microscopic mechanism of dielectric breakdown in SiO₂ films: An insight from multi-scale modeling,” *J. Appl. Phys.* **121**(15), 155101 (2017).
- ¹¹F. M. Puglisi, L. Larcher, A. Padovani, and P. Pavan, “A complete statistical investigation of RTN in HfO₂-based RRAM in high resistive state,” *IEEE Trans. Electron Devices* **62**(8), 2606–2613 (2015).
- ¹²F. M. Puglisi, L. Larcher, A. Padovani, and P. Pavan, “Anomalous random telegraph noise and temporary phenomena in resistive random access memory,” *Solid State Electron.* **125**, 204–213 (2016).
- ¹³T. Nagumo, K. Takeuchi, T. Hase, and Y. Hayashi, “Statistical characterization of trap position, energy, amplitude and time constants by RTN measurement of multiple individual traps,” in *Technical Digest—International Electron Devices Meeting, IEDM* (IEDM, 2010), pp. 628–631.
- ¹⁴E. R. Hsieh, H. W. Cheng, Z. H. Huang, C. H. Chuang, S. P. Yang, and S. S. Chung, “A pulsed RTN transient measurement technique: Demonstration on the understanding of the switching in resistance memory,” in *IEEE International Reliability Physics Symposium Proceedings, April 2020* (IEEE, 2020), pp. 8–11.
- ¹⁵B. Stampfer, A. Grill, and M. Waltl, “Advanced electrical characterization of single oxide defects utilizing noise signals,” in *Noise in Nanoscale Semiconductor Devices* (Springer, Cham, 2020), pp. 229–257.
- ¹⁶T. Nagumo, K. Takeuchi, S. Yokogawa, K. Imai, and Y. Hayashi, “New analysis methods for comprehensive understanding of random telegraph noise,” in *Technical Digest—International Electron Devices Meeting, IEDM* (IEDM, 2009), pp. 759–762.
- ¹⁷F. M. Puglisi and P. Pavan, “Factorial hidden Markov model analysis of random telegraph noise in resistive random access memories,” *ECTI Trans. Electr. Eng., Electron. Commun.* **12**(1), 24–29 (2014).
- ¹⁸S. Vecchi, P. Pavan, and F. M. Puglisi, “The impact of electrostatic interactions between defects on the characteristics of random telegraph noise,” in *IEEE Transactions on Electron Devices* (IEEE, 2022).
- ¹⁹See <https://www.appliedmaterials.com/products/applied-mdlx-ginestra-simulation-software> for information about Applied Material’s Ginestra simulation software.
- ²⁰F. M. Puglisi, L. Larcher, A. Padovani and P. Pavan, “Characterization of anomalous Random Telegraph Noise in Resistive Random Access Memory,” *2015 45th European Solid State Device Research Conference (ESSDERC)*, Graz, Austria, (IEEE, 2015), pp. 270–273.
- ²¹M. Herrmann and A. Schenk, “Field and high-temperature dependence of the long term charge loss in erasable programmable read only memories: Measurements and modeling,” *J. Appl. Phys.* **77**(9), 4522–4540 (1995).
- ²²L. Larcher, “Statistical simulation of leakage currents in MOS and flash memory devices with a new multiphonon trap-assisted tunneling model,” *IEEE Trans. Electron Devices* **50**(5), 1246–1253 (2003).
- ²³A. Padovani *et al.*, “Statistical modeling of leakage currents through SiO₂ high-k dielectrics stacks for non-volatile memory applications,” in *IEEE CFP08RPS-CDR 46th Annual International Reliability Physics Symposium, Phoenix* (IEEE, 2008), pp. 616–620.
- ²⁴L. Vandelli, L. Larcher, D. Veksler, A. Padovani, G. Bersuker, and K. Matthews, “A charge-trapping model for the fast component of positive bias temperature instability (PBT) in high-κ gate-stacks,” *IEEE Trans. Electron Devices* **61**(7), 2287–2293 (2014).
- ²⁵D. V. Lang and C. H. Henry, “Nonradiative capture and recombination by multiphonon emission in GaAs and GaP,” *Phys. Rev. B* **15**(2), 989–1016 (1977).
- ²⁶J. Markham, “Interaction of normal modes with electron traps,” *Rev. Mod. Phys.* **31**(4), 956–989 (1959).
- ²⁷K. Huang and A. Rhys, “Theory of light absorption and non-radiative transitions in F-centres,” in *Proceedings of the Royal Society of London. Series A. Mathematical and Physical Sciences*, Vol. 204 (1078)(1950), 74–92 (2000).
- ²⁸L. Vandelli, A. Padovani, L. Larcher, R. G. Southwick, W. B. Knowlton, and G. Bersuker, “A physical model of the temperature dependence of the current through SiO₂/HfO₂ stacks,” *IEEE Trans. Electron Devices* **58**(9), 2878–2887 (2011).

- ²⁹A. S. Foster, F. Lopez Gejo, A. L. Shluger, and R. M. Nieminen, “Vacancy and interstitial defects in hafnia,” *Phys. Rev. B* **65**(17), 1741171–17411713 (2002).
- ³⁰N. Capron, P. Broqvist, and A. Pasquarello, “Migration of oxygen vacancy in HfO₂ and across the HfO₂/SiO₂ interface: A first-principles investigation,” *Appl. Phys. Lett.* **91**(19), 192905 (2007).
- ³¹J. W. Strand, J. Cottom, L. Larcher, and A. L. Shluger, “Effect of electric field on defect generation and migration in HfO₂,” *Phys. Rev. B* **102**(1), 1–8 (2020).
- ³²S. Vecchi, P. Pavan, and F. M. Puglisi, “The relevance of trapped charge for leakage and random telegraph noise phenomena,” in *IEEE International Reliability Physics Symposium* (IEEE, 2022), pp. 4–9.
- ³³F. M. Puglisi, P. Pavan, A. Padovani, and L. Larcher, “A compact model of hafnium-oxide-based resistive random access memory,” in *ICICDT 2013—International Conference on IC Design and Technology, Proceedings* (IEEE, 2013), pp. 85–88.
- ³⁴IEEE, International Roadmap for Devices and Systems (IRDS™) 2021 Edition: More Moore, available at <https://irds.ieee.org/editions/2021/more-moore>.
- ³⁵A. Padovani *et al.*, “Reliability of non-volatile memory devices for neuromorphic applications: A modeling perspective (invited),” in *IEEE International Reliability Physics Symposium Proceedings, March 2022* (IEEE, 2022), pp. 3C41–3C410.
- ³⁶Y. Son, T. Kang, S. Park, and H. Shin, “A simple model for capture and emission time constants of random telegraph signal noise,” *IEEE Trans. Nanotechnol.* **10**(6), 1352–1356 (2011).
- ³⁷F. M. Puglisi and P. Pavan, “Guidelines for a reliable analysis of random telegraph noise in electronic devices,” *IEEE Trans. Instrum. Meas.* **65**(6), 1435–1442 (2016).
- ³⁸T. Grasser, “Stochastic charge trapping in oxides: From random telegraph noise to bias temperature instabilities,” *Microelectron. Reliab.* **52**(1), 39–70 (2012).
- ³⁹A. Ranjan *et al.*, “CAFM based spectroscopy of stress-induced defects in HfO₂ with experimental evidence of the clustering model and metastable vacancy defect state,” in *2016 IEEE International Reliability Physics Symposium (IRPS)*, Pasadena, CA, USA (IEEE, 2016), pp. 7A-4-1–7A-4-7.
- ⁴⁰Y. Qiu, R. Wang, J. Ji, and R. Huang, “Deep understanding of oxide defects for stochastic charging in nanoscale MOSFETs,” in *2014 Silicon Nanoelectronics Workshop (SNW), Honolulu, HI, USA* (IEEE, 2014), pp. 1–2.
- ⁴¹A. Grill *et al.*, “Characterization and modeling of single defects in GaN/AlGaIn fin-MIS-HEMTs,” in *IEEE International Reliability Physics Symposium Proceedings* (IEEE, 2017), pp. 3B5.1–3B5.5.
- ⁴²S. Vecchi, P. Pavan, and F. M. Puglisi, “Defects motion as the key source of random telegraph noise instability in hafnium oxide,” in *ESSDERC 2022—IEEE 52nd European Solid-State Device Research Conference (ESSDERC)*, Milan, Italy (IEEE, 2022), pp. 368–371.
- ⁴³S. Vecchi, P. Pavan, and F. M. Puglisi, “A unified framework to explain random telegraph noise complexity in MOSFETs and RRAMs,” *IEEE IRPS* (IEEE, 2023) (to be published).